Environmental Science Nano

ROYAL SOCIETY OF CHEMISTRY

PAPER

View Article Online
View Journal | View Issue

Cite this: *Environ. Sci.: Nano*, 2021, 8, 3711

Biomimetically synthesized luminescent Tb^{3+}-doped fluorapatite/agar nanocomposite for detecting UO_2^{2+}, Cu^{2+}, and Cr^{3+} ions†

Hongjuan Liu,[ab] Xianli Wang,[a] Thulitha Abeywickrama,[a] Forough Jahanbazi,[a] Zefu Min,[b] ZhengRong Lee,[c] Jeff Terry [cd] and Yuanbing Mao *[a]

Received 17th July 2021,
Accepted 18th October 2021

DOI: 10.1039/d1en00648g

rsc.li/es-nano

Radionuclides and heavy metal ions have become the main harmful pollutants in the environment. Developing sensitive and rapid methods to detect them from natural water or wastewater is important to reduce their exposure risks. In this study, a novel luminescent Tb^{3+}-doped fluorapatite/agar nanocomposite (Tb-FAP/agar) has been synthesized *via* a facile and green synthetic route through an environmentally friendly biomineralization process using agar as a template. This nanocomposite is the first luminescent fluorapatite for detecting UO_2^{2+}, Cu^{2+}, and Cr^{3+} ions in water with high selectivity and sensitivity based on luminescence turn-off effects. The detection limits of the Tb-FAP/agar for UO_2^{2+} (7.95 nM), Cu^{2+} (3.94 nM), and Cr^{3+} (1.67 nM) are much lower than the permissible limits in drinking water defined by the United States Environmental Protection Agency (USEPA). Furthermore, the luminescence detection mechanisms for UO_2^{2+}, Cu^{2+}, and Cr^{3+} ions were speculated. Our study provides insight into developing biodegradable rare earth doped fluorapatite probes for the detection of both radioactive and nonradioactive ions.

Environmental significance

Radionuclides and heavy metal ions have become the main harmful pollutants in the environment. Developing sensitive and rapid methods to detect them from natural water or wastewater is important to reduce their exposure risks. Here we synthesized a luminescent Tb^{3+}-doped fluorapatite/agar nanocomposite *via* an environmentally friendly biomineralization process and demonstrated its detection for UO_2^{2+}, Cu^{2+}, and Cr^{3+} ions in water with high selectivity and sensitivity based on luminescence turn-off effects. Its detection limits for these three ions are much lower than the permissible limits in drinking water defined by the United States Environmental Protection Agency (USEPA). Our findings indicated that luminescent nanocomposites can be environmentally friendly designed and explored as potential luminescence sensors for environmental monitoring applications.

1. Introduction

Hydroxyapatite [$(Ca_{10}(PO_4)_6(OH)_2$, HAP] is the main inorganic ingredient of vertebrate hard tissues such as bones and teeth.[1,2] It is a biodegradable, eco-friendly material with excellent biocompatibility and bioactivity. Moreover, HAP is a good host lattice for doping of rare earth (RE) ions. This is because the ionic radii of RE ions are close to that of Ca^{2+}, enabling their easy substitution for Ca^{2+} in HAP. HAP materials doped with RE ions such as Tb^{3+} and Eu^{3+} have potential applications as luminescent probes due to their excellent luminescence characteristics.[3,4] The fluoride ion (F^-) is usually used for replacing the hydroxyl (–OH) group of HAP to form calcium fluorapatite [$Ca_{10}(PO_4)_6F_2$, FAP] to further improve the luminescence properties because of the absence of the OH^- group that has a possible quenching effect on the luminescence of RE ions.[1,5] Meanwhile, the F^- ion generates lower vibration energy and promotes efficient luminescence conversion.[6,7]

Synthesis methods of HAP mainly include chemical precipitation,[8] sol–gel,[9,10] combustion,[11] hydrothermal,[12] microemulsion,[13] and biomineralization processes.[14] Among these methods, the biomimetic synthesis method operating under mild environment conditions does not need poisonous reagents, avoiding relying on high temperature, high pressure, strong acids and alkalis and harsh reaction

[a] *Department of Chemistry, Illinois Institute of Technology, 3101 South Dearborn Street, Chicago, IL 60616, USA. E-mail: ymao17@iit.edu; Tel: +1 312 567 3815*
[b] *School of Nuclear Science and Technology, University of South China, Hengyang, 421001, China*
[c] *Department of Physics, Illinois Institute of Technology, 3101 South Dearborn Street, Chicago, IL 60616, USA*
[d] *Department of Mechanical Materials, and Aerospace Engineering, Illinois Institute of Technology, 3101 South Dearborn Street, Chicago, IL 60616, USA*

† Electronic supplementary information (ESI) available: Information related to FTIR, XPS, TGA, XRD, PL lifetime and fitting parameters, PL intensity after and before treatment with different metal ions, UV-vis spectra, and determination of the limit of detection (LOD) value. See DOI: 10.1039/d1en00648g

conditions. This method has excellent advantages of simple operation, low energy consumption, environmental friendliness and good material tuning, thus arousing widespread attention.[15–18] The biomimetic synthesis is a process mimicking the formation of inorganic materials by biomineralization under the modulation of organic matter, such as polysaccharides, proteins, nucleic acids, *etc.*[19,20] Interaction between polysaccharides and metal ions plays an important role in the biomineralization of inorganic materials,[21–24] and using agar as a polysaccharide template to simulate HAP formation could be closer to the biomineralization process.

Radionuclides and heavy metal ions have become the main harmful pollutants in the environment. Uranium contamination has aroused global concern because it could be readily caused by nuclear accidents and various nuclear industries such as nuclear power stations, uranium mining and processing, *etc.* The ingestion or inhalation of uranium could lead to urinary system disease, disruption of bioactive molecules, irreversible kidney damage, and DNA or immune system damage due to the chemotoxicity and radiotoxicity of uranium.[25]

Cr^{3+} and Cu^{2+} are essential trace elements for human health. Their excess or deficiency may cause several abnormalities in human health. Chromium deficiency increases the risk factors associated with diabetes and cardiovascular diseases. Excessive Cr^{3+} exposure and intake lead to mutations or malignant cells.[26,27] Exposure to excessive Cu^{2+} could cause serious liver or kidney damage, gastrointestinal disorders, and various neurological diseases, such as Parkinson's disease, Alzheimer's disease, and Wilson's disease.[28,29] Hence, developing sensitive methods to detect UO_2^{2+}, Cu^{2+}, and Cr^{3+} from natural water or wastewater is important to reduce the risk of exposure.

Current sensing techniques for metallic ion detection, such as inductively coupled plasma mass spectrometry (ICP-MS),[30] atomic absorption spectroscopy (AAS),[31] and capillary electrophoresis,[32] usually require complicated sample preparation, expensive instrumentation, and/or sophisticated operation, making them difficult for real-time and on-site detection. Hence, luminescence detection has become a very popular analytical method for metal ion detection due to its high sensitivity and selectivity and real-time and rapid response.[33–36] Luminescent sensors, such as MOF-based sensors,[37–40] carbon dot-based sensors,[34,41] and polymeric sensors,[42] have been developed for metallic ion detection with good detection performance. RE-doped FAP, as an eco-friendly material with outstanding luminescence properties, is envisaged by us to have the potential to be developed as a luminescent probe for metallic ion detection, although at present there is no relevant research about RE-doped FAP for metallic ion detection as far as we know.

Herein, a novel luminescent Tb^{3+}-doped fluorapatite/agar nanocomposite (Tb-FAP/agar) for detecting UO_2^{2+}, Cu^{2+}, and Cr^{3+} ions was synthesized by an environmentally friendly biomimetic process (Scheme 1). To the best of our knowledge, this luminescent fluorapatite nanocomposite for detection of metal ions has never been reported before. In this work, the detection of UO_2^{2+}, Cu^{2+}, and Cr^{3+} ions was systematically studied. Furthermore, the luminescence quenching mechanisms of the Tb-FAP/agar sample for UO_2^{2+}, Cu^{2+}, and Cr^{3+} ions were studied by FTIR, XPS, UV-vis absorption spectroscopy, luminescence excitation and emission spectroscopy, and luminescence lifetime measurements. This work not only paves a way but also provides a valuable basis for RE-doped FAP luminescent probes for the detection of both radioactive and nonradioactive ions in water.

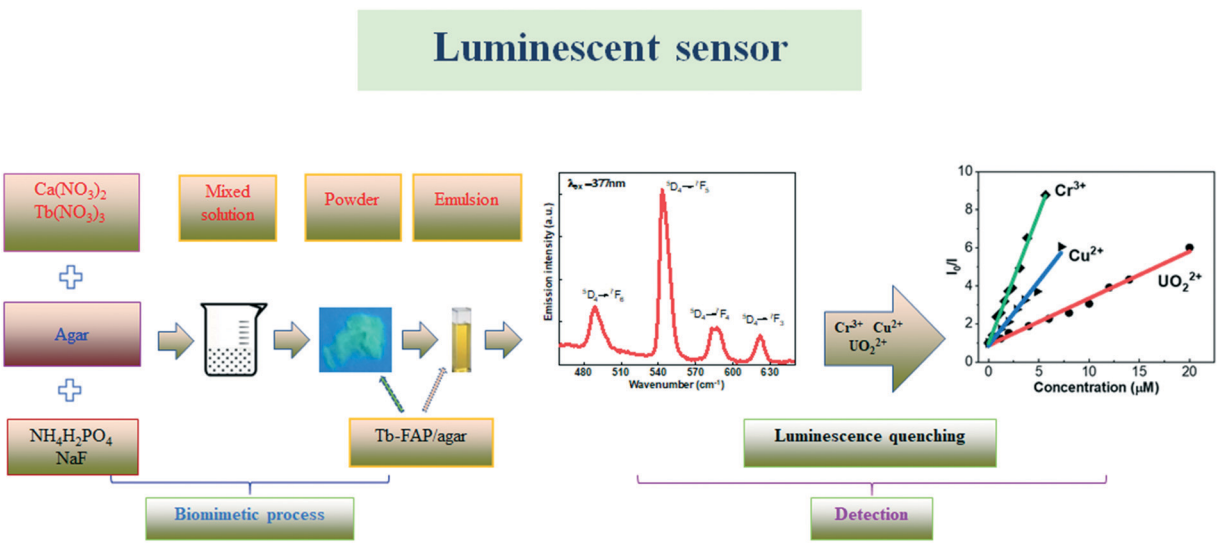

Scheme 1 Schematic for the biomimetic process of the Tb-FAP/agar sample and the subsequent detection of UO_2^{2+}, Cu^{2+}, and Cr^{3+} ions in aqueous solution.

2. Experimental section

2.1. Chemicals and materials

Terbium nitrate [$Tb(NO_3)_3{\cdot}5H_2O$], aluminum nitrate [$Al(NO_3)_3{\cdot}9H_2O$], sodium nitrate ($NaNO_3$), sodium hydroxide (NaOH) and agar were purchased from Sigma Aldrich. Potassium nitrate (KNO_3), cerium nitrate [$Ce(NO_3)_3{\cdot}6H_2O$], lanthanum nitrate [$La(NO_3)_3{\cdot}6H_2O$], strontium nitrate [$Sr(NO_3)_2$], zinc nitrate [$Zn(NO_3)_2{\cdot}6H_2O$] and absolute ethanol were obtained from Alfa Aesar. Gadolinium nitrate [$Gd(NO_3)_3{\cdot}6H_2O$] and chromium nitrate [$Cr(NO_3)_3{\cdot}9H_2O$] were purchased from Acros Organics. Calcium nitrate [$Ca(NO_3)_2{\cdot}4H_2O$], copper nitrate [$Cu(NO_3)_2{\cdot}3H_2O$] and sodium fluoride (NaF) were obtained from Fisher Scientific. Monobasic ammonium phosphate ($NH_4H_2PO_4$) and uranyl nitrate $(UO_2)(NO_3)_2$ were received from Fluka and United Nuclear Corporation, respectively. All chemicals of analytical grade were used without further purification. All the solutions in this work were prepared with deionized water.

2.2. Synthesis of luminescent nanocomposites

The Tb-FAP/agar was prepared by a biomimetic synthesis process. Briefly, 0.912 g of $Ca(NO_3)_2{\cdot}4H_2O$ and 0.134 g of $Tb(NO_3)_3{\cdot}5H_2O$ were dissolved in deionized water to form 25 mL of solution #1. NaOH (1 mol L^{-1}) was added into solution #1 to adjust its pH to 10. Also, 0.16 g of agar was dissolved in deionized water by heating at 100 °C under magnetic stirring at 500 rpm to form 20 mL of solution #2 of 0.8% agar. Moreover, 0.2099 g of NaF and 0.288 g of $NH_4H_2PO_4$ were dissolved in deionized water to form 25 mL of solution #3. 1 mol L^{-1} NaOH(aq) was added into solution #3 to adjust its pH to 10. Then, solution #1 was added dropwise into solution #2 under stirring at 500 rpm. After mixing solutions #1 and #2, solution #3 was also introduced into the mixture dropwise. After adjusting the pH of the entire mixture to 10 using 1 mol L^{-1} NaOH(aq), the mixture solution was magnetically stirred at 800 rpm at 80 °C for another 4 h. Finally, the precipitate was separated by centrifugation at 6500 rpm, washed four times with ethanol and deionized water, and then dried at 70 °C overnight. For comparative purposes, Tb-doped FAP was also synthesized by following the same process but without adding agar and named Tb-FAP agar free, while Tb-doped hydroxyapatite/agar (Tb-HAP/agar) was prepared without adding NaF during the synthesis.

2.3. Characterization and instrumentation

X-ray diffraction (XRD) measurements were performed on a Bruker D2 Phaser diffractometer with Cu Kα at a scanning rate of 1° min^{-1} in the 2θ range from 10° to 80°. The composition of the nanocomposites was characterized with a physical electronic (PHI) model 5600 X-ray photoelectron spectrometer (XPS) equipped with an Al K_α monochromatic X-ray source. The photon energy was 1486.7 eV and the pass energy used for the high-resolution core level scans was 11.75 eV, resulting in an energy resolution of 0.17 eV. The morphology of the sample was obtained using a JSM-6701F scanning electron microscope. The Fourier transform infrared spectra (FT-IR) were obtained with a Perkin Elmer spectrum two spectrometer in the range of 400–4000 cm^{-1}. Thermogravimetric analysis (TGA) was performed using a Mettler Toledo TGA instrument under an air atmosphere with a flow rate of 30 ml min^{-1} at a heating rate of 10° min^{-1}. Ultraviolet-visible (UV-vis) absorption was recorded using a Beckman Coulter DU 800 ultraviolet-visible spectrophotometer. Photoluminescence measurements were performed with an FLS1000 spectrofluorometer. All the emission spectra were recorded using the FLS1000 system from Edinburgh Instrument with a steady state Xe lamp as the excitation source. Luminescence lifetime measurements were performed using the same FLS1000 with a pulsed Xe source.

2.4. Photoluminescence measurements and sensing properties for metal ions

Emulsions of the Tb-FAP/agar were prepared by dissolving the Tb-FAP/agar samples in deionized water. The pH of the emulsions was adjusted by using 1 M NaOH and 1 M HCl solutions to be in the pH range from 1 to 12. The luminescence spectra of these emulsions (2.5 mL, 0.1 mg mL^{-1}) in quartz cuvettes were recorded to obtain the luminescence properties of the Tb-FAP/agar at different pH values. The emission spectra of the Tb-FAP/agar, Tb-FAP agar free, and Tb-HAP/agar emulsions (2.5 mL, 0.1 mg mL^{-1}) in quartz cuvettes were measured to compare the luminescence intensity of these three samples. To investigate its selectivity properties for metal ions, emulsions of the Tb-FAP/agar sample (2.5 mL, 0.1 mg mL^{-1}) in quartz cuvettes were mixed with the corresponding aqueous solutions containing various kinds of metal ions: (10 μL, 0.01 mmol) of $Tb(NO_3)_3{\cdot}5H_2O$, $Al(NO_3)_3{\cdot}9H_2O$, $NaNO_3$, KNO_3, $Ce(NO_3)_3{\cdot}6H_2O$, $La(NO_3)_3{\cdot}6H_2O$, $Sr(NO_3)_2$, $Zn(NO_3)_2{\cdot}6H_2O$, $Gd(NO_3)_3{\cdot}6H_2O$, $Cr(NO_3)_3{\cdot}9H_2O$, $Ca(NO_3)_2{\cdot}4H_2O$, $Cu(NO_3)_2{\cdot}3H_2O$, and $(UO_2)(NO_3)_2$, by means of a micro-pipette. To further examine the luminescence response of the Tb-FAP/agar sample to UO_2^{2+}, Cu^{2+}, and Cr^{3+} ions, the Tb-FAP/agar emulsions (2.5 mL, 0.1 mg mL^{-1}) were mixed with UO_2^{2+}, Cu^{2+}, and Cr^{3+} at different concentrations. After the metal ions were mixed with the Tb-FAP/agar emulsions, the emulsions were shaken for 10 min before PL spectra were taken. The luminescence properties of the Tb-FAP/agar with different metal ions and the pure Tb-FAP/agar emulsion were recorded using the FLS1000 and compared.

3. Results and discussion

3.1. Characterization

The morphology of the Tb-FAP/agar sample was examined by SEM. The SEM image shown in Fig. S1† indicates that the as-prepared Tb-FAP/agar is composed of numerous nanoscale particles. The FT-IR spectrum of the Tb-FAP/agar nanocomposite is shown in Fig. 1a. The broad band at 3420 cm^{-1} and the weaker signal at around 1634 cm^{-1} were due to O–H vibration and the H–O–H bending mode of water absorbed in the sample, respectively.[5,43] The presence of agar on the

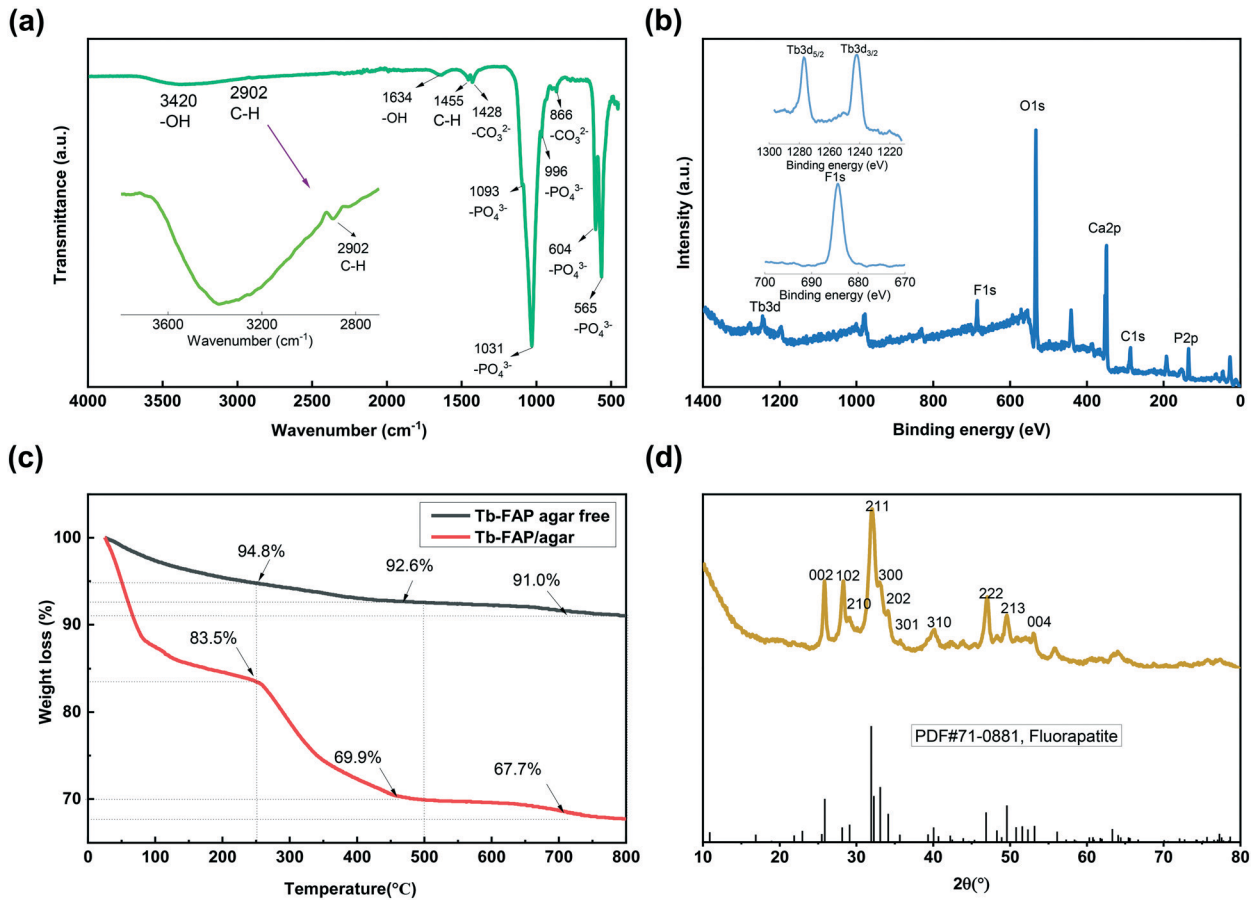

Fig. 1 (a) The FT-IR spectrum of the Tb-FAP/agar nanocomposite. (b) Survey scan of the XPS spectrum of the Tb-FAP/agar nanocomposite with the detailed scans for F 1s and Tb 3d as insets. (c) The TGA plots of the Tb-FAP/agar and Tb-FAP agar free nanocomposite samples. (d) XRD pattern of the Tb-FAP/agar nanocomposite.

surface of the Tb-FAP/agar sample was also detected in the FTIR spectrum of the sample. The weak bands at 1455 cm^{-1} and 2902 cm^{-1} (Fig. 1a, magnified in the inset) correspond to the scissoring vibrations and stretching vibrations of the C–H groups from agar.[5,43] The FT-IR spectrum showed the typical active vibrational bands related to the phosphate groups (PO_4^{3-}). Specifically, the bands at 565 cm^{-1} and 604 cm^{-1} (ν_4 – the triply degenerate) were associated with vibrational PO_4^{3-} groups, the band at 966 cm^{-1} (ν_1 – the non-degenerate) was assigned to symmetric stretching of PO_4^{3-} groups, and the bands at 1031 cm^{-1} and 1093 cm^{-1} (ν_3 – the triply degenerate) were assigned to the asymmetric stretching mode of PO_4^{3-} groups.[1,7,44] The bands at 1428 and 866 cm^{-1} were ascribed to the stretching vibrations of CO_3^{2-} groups, indicating the presence of carbonate ions replacing phosphate ions.[5,43] The corresponding Tb-HAP/agar and Tb-FAP agar free samples in Fig. S2† also showed the characteristic peaks of hydroxyapatite and fluorapatite, respectively. The signals of the OH groups of the Tb-HAP/agar were stronger than those of the Tb-FAP/agar as the OH groups of the Tb-HAP/agar were not substituted by F^- ions. The peak at around 2902 cm^{-1} representing the C–H group did not appear in the spectrum of the Tb-FAP agar free sample as it contained no agar.

The XPS spectrum of the Tb-FAP/agar nanocomposite is shown in Fig. 1b. For this nanocomposite, the characteristic peaks of C 1s, Ca 2p, P 2p, O 1s, F 1s and Tb 3d were all detected. The F 1s spectrum of the Tb-FAP/agar (Fig. 1b, inset) showed a characteristic peak at 684.5 eV. The Tb 3d spectrum of the Tb-FAP/agar (Fig. 1b, inset) showed two characteristic peaks at about 1242.35 eV and 1277.15 eV, which were identified as Tb $3d_{5/2}$ and Tb $3d_{3/2}$, respectively. These results confirmed the existence of F^- and Tb^{3+} ions in the as-prepared Tb-FAP/agar sample. However, the F 1s peak was not found in the XPS spectrum of the Tb-HAP/agar (Fig. S3†).

The TGA plots of the Tb-FAP/agar and Tb-FAP agar free samples are shown in Fig. 1c. The Tb-FAP/agar free sample showed a weight loss of 5.2% at 25–250 °C which can be ascribed to the loss of absorbed water with the increase of temperature. The loss of water (16.5%) for the Tb-FAP/agar sample was higher than that found for the Tb-FAP agar free sample (5.2%). This can be attributed to the agar-functionalized samples being able to absorb more water due to the hydrophilicity of agar. The weight loss between 250 and 500 °C for the Tb-FAP agar free sample was just 2.2%, which is much lower than those for the Tb-FAP/agar (13.6%,

Fig. 1c) and Tb-HAP/agar samples (15.3%, Fig. S4†). This should be related to the decomposition of the agar, which occurs in this range of temperature as shown in Fig. S4.† This result indicated that agar was grafted onto FAP, which was in good agreement with the FTIR observations (Fig. 1a). Finally, the slight weight losses observed at 500–800 °C (2.2% from the Tb-FAP/agar sample and 1.6% from the Tb-FAP agar-free sample) should be related to the dehydroxylation and defluorination of the apatite structures.[5]

The XRD pattern of the Tb-FAP/agar sample is presented in Fig. 1d. The characteristic diffraction peaks at 2θ (°) = 25.830, 28.026, 28.248, 31.98, 32.010, 32.709, 40.136, 46.970, and 49.538 can be assigned to the crystal planes of (002), (102), (210), (211), (300), (202), (310), (222), and (213), respectively. It was highly consistent with the standard FAP reference [PDF#71-0881]. The nanocomposite exhibited the pure hexagonal crystal structure of typical FAP (space group: $P6_3/m$). No other peaks of additional phases existed, demonstrating that Tb^{3+} was effectively incorporated into the FAP lattice. Compared to the Tb-HAP/agar sample which matched the standard HAP reference [PDF#86-0740] (Fig. S5†), the peaks of the Tb-FAP/agar were much sharper than those of the Tb-HAP/agar. This result indicated that the crystallinity degree of the Tb-FAP/agar was higher than that of the Tb-HAP/agar, which could be caused by the F^- substitution of the –OH group.[1]

3.2. Photoluminescence properties

The effect of pH on the luminescence intensity of the Tb-FAP/agar sample was investigated in the pH range from 1 to 12. As shown in Fig. S6,† the luminescence intensity of the Tb-FAP/agar emulsions is the highest in the sample solution at pH = 7. The luminescence intensity of the emulsions decreased with either decreasing pH (pH < 7) or increasing pH (pH > 7), which demonstrates that the luminescence intensity of the Tb-FAP/agar emulsions is dependent on the pH value. The luminescence intensity of the Tb-FAP/agar in an acidic environment is weaker than that in neutral and alkaline environments, which is because the samples could partially dissolve in an acidic environment.[45] Thus, the sample is more suitable for applications in neutral and alkaline environments. As the luminescence intensity of the Tb-FAP/agar was the highest in the sample solution at pH = 7, all the subsequent experiments were performed at a pH of 7.

The emission spectra of the Tb-FAP/agar, Tb-FAP agar free and Tb-HAP/agar samples are shown in Fig. 2a. The results indicated that these samples with Tb^{3+} excited at 377 nm by UV light can produce characteristic luminescence in the wavelength range of 450 nm and 650 nm with the maximum emission wavelength of 543 nm. The peaks at 489 nm, 543 nm, 587 nm, and 621 nm corresponded to $^5D_4 \rightarrow {}^7F_6$, $^5D_4 \rightarrow {}^7F_5$, $^5D_4 \rightarrow {}^7F_4$, and $^5D_4 \rightarrow {}^7F_3$ transitions, respectively. The emission intensity of the Tb-FAP/agar sample was about five times higher than that of the Tb-HAP/agar sample. Such a difference in emission intensity was further confirmed by the longer luminescence lifetime obtained from the Tb-FAP/agar sample (1208.37 μs) when compared with that from the Tb-HAP/agar sample (1056.97 μs) as shown in Fig. S7 and Table S1.† This could be due to the presence of the OH^- group in the Tb-HAP/agar sample, which was well known to lead to high vibrational frequency around activators and reduce luminescence efficiency or even quench emission, while F^- ions have lower vibrational energy than OH^- groups.[1] This difference favors luminescence transition from FAP over HAP to Tb^{3+} ions. Therefore, in the matrix of apatite, the F^- substitution of the OH^- group could decrease the luminescence quenching of Tb^{3+} ions and promote luminescence conversion.[1]

In addition, the emission intensity of the Tb-FAP/agar sample was stronger than that of the Tb-FAP agar free sample. This difference in the emission intensity was further confirmed by the result that the luminescence lifetime of the Tb-FAP/agar sample (1208.37 μs) is longer than that of the Tb-FAP agar free sample (1177.91 μs) as shown in Fig. S7 and

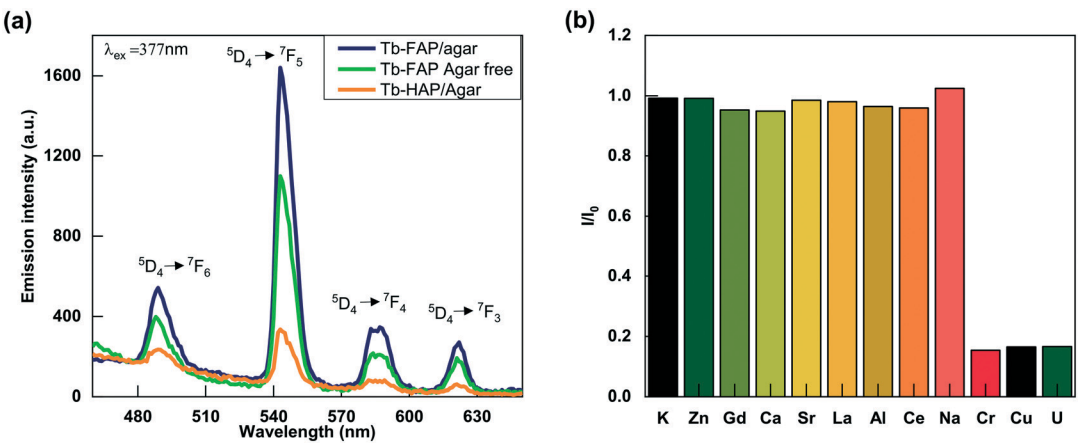

Fig. 2 (a) The emission spectra of the Tb-FAP/agar, Tb-FAP agar free, and Tb-HAP/agar samples. (b) Luminescence intensity of the $^5D_4 \rightarrow {}^7F_5$ transitions (543 nm) of the Tb-FAP/agar (2.5 mL) with different metal ions (10 μL, 0.01 M).

Table S1.† This could be because agar played a role as the template and dispersant in the biomimetic synthesis process, resulting in higher luminescence of the Tb-FAP/agar sample. Similar results reported that the templates of biomimetic synthesis could enhance the luminescence properties of Ag_2Se quantum dots.[46] Therefore, both F^- ions and agar can improve the luminescence intensity of the Tb-FAP/agar nanocomposite.

3.3. Sensing properties for metal ions

Due to its high luminescence intensity, we investigated the Tb-FAP/agar sample's detection properties for metal ions by exploring its luminescence change upon the addition of several different metal ions in aqueous solution (Fig. 2b). It was obvious that the Tb-FAP/agar emulsions exhibited a luminescence quenching effect on UO_2^{2+}, Cu^{2+}, and Cr^{3+} ions while they showed only slight weakening or even enhancement of the luminescence intensity at different degrees with the other tested metal ions. Moreover, increasing the amount of the other metal ions (K^+, Zn^{2+}, Gd^{3+}, Ca^{2+}, Sr^{2+}, La^{3+}, Al^{3+}, Ce^{3+}, Na^+) by a factor of 10 by changing the volume of their aqueous solutions from 10 μL to 100 μL with the same concentration of 0.01 M only slightly affected the luminescence intensity (Fig. S8†).

Fig. 3 shows the concentration effect of the UO_2^{2+}, Cu^{2+}, and Cr^{3+} ions on the luminescence response of the Tb-FAP/agar sample. It could be observed that the luminescence intensity of the Tb-FAP/agar decreased with increasing concentration of UO_2^{2+}, Cu^{2+}, and Cr^{3+} ions while the luminescence intensity of the Tb-FAP/agar emulsion without adding UO_2^{2+}, Cu^{2+}, and Cr^{3+} ions almost did not change within 3 days (Fig. S9†). These results indicated that the luminescence properties of the Tb-FAP/agar were stable and confirmed that the luminescence intensity decrease of the Tb-FAP/agar was caused by the concentration change of the UO_2^{2+}, Cu^{2+} and Cr^{3+} ions, not by the photo-bleaching of the Tb-FAP/agar sample.

To reveal the luminescence sensitivity of the Tb-FAP/agar sample to the UO_2^{2+}, Cu^{2+}, and Cr^{3+} ions, their luminescence quenching constants were quantified by the Stern–Volmer equation:

$$I_0/I = K_{SV}[Q] + 1 \quad (1)$$

where I_0 and I are the original luminescence intensity and luminescence intensity of the Tb-FAP/agar in the presence of the UO_2^{2+}, Cu^{2+}, and Cr^{3+} ions, respectively, K_{SV} is the Stern–Volmer quenching constant, and [Q] is the molar concentration of the UO_2^{2+}, Cu^{2+}, and Cr^{3+} ions. Linear responses were obtained from the plots of the I_0/I against the concentration of the UO_2^{2+}, Cu^{2+} and Cr^{3+} ions (insets of Fig. 3a–c, respectively), indicating the dynamic nature of the luminescence quenching.[47]

The obtained luminescence quenching constants (K_{SV}) of the Tb-FAP/agar sample were 2.47×10^5 M^{-1} for UO_2^{2+}, 6.77×10^5 M^{-1} for Cu^{2+}, and 1.37×10^6 M^{-1} for Cr^{3+}. The limits of detection (LOD) of the Tb-FAP/agar sample for the UO_2^{2+}, Cu^{2+}, and Cr^{3+} ions were calculated using the formula 3σ/slope.[37,48] The details of the LOD determination are shown in Fig. S10.† The calculated LOD values of the Tb-FAP/agar sample were 7.95 nM (2.15 μg L^{-1}) for UO_2^{2+}, 3.94 nM (0.25 μg L^{-1}) for Cu^{2+}, and 1.67 nM (0.087 μg L^{-1}) for Cr^{3+}, which were much lower than the contamination limits of uranium (30 μg L^{-1}),[37] copper (2 mg L^{-1}),[49] and chromium (100 μg L^{-1})[50] in drinking water defined by the United States Environmental Protection Agency (USEPA). The LOD values of

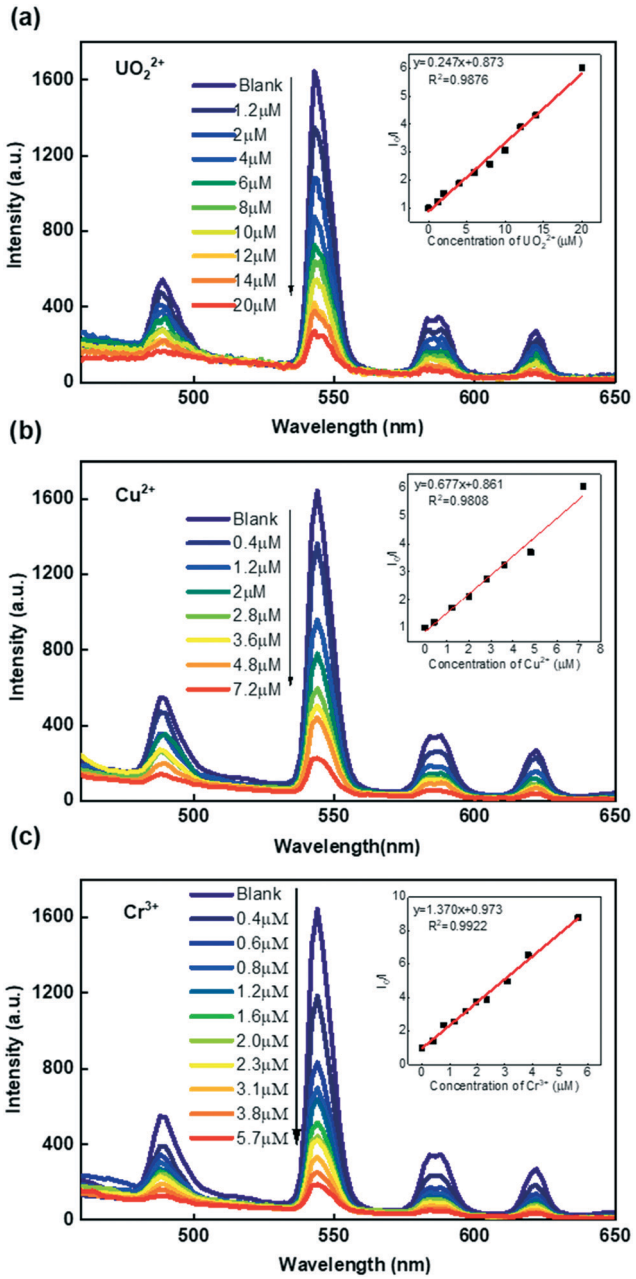

Fig. 3 The concentration effect of (a) UO_2^{2+}, (b) Cu^{2+}, and (c) Cr^{3+} ions on the PL intensity of Tb-FAP/agar (λ_{ex} = 377 nm). Insets show the corresponding fitting curves of the PL intensity of Tb-FAP/agar at 543 nm with the concentration of (a) UO_2^{2+}, (b) Cu^{2+}, and (c) Cr^{3+} ions.

the Tb-FAP/agar sample for the UO_2^{2+}, Cu^{2+}, and Cr^{3+} ions are also lower than those of most reported luminescent sensors as shown in Table 1. The large K_{SV} and low LOD values indicated the excellent selectivity and sensitivity of the Tb-FAP/agar sample, which would become an effective luminescent sensor for detecting UO_2^{2+}, Cu^{2+}, and Cr^{3+} ions. Moreover, the calculated sensing repeatability of the Tb-FAP/agar to Cu^{2+}, Cr^{3+}, and UO_2^{2+} ions is 2.09%, which indicates its desirable luminescence response stability.

3.4. Luminescence quenching mechanism for ion detection

The luminescence quenching mechanism of the Tb-FAP/agar sample for the UO_2^{2+}, Cu^{2+}, and Cr^{3+} ions was expounded by FTIR, XPS, UV-vis absorption spectroscopy, luminescence excitation and emission spectroscopy, and luminescence lifetime measurements. As shown in Fig. S11,† the characteristic UO_2^{2+} peak appeared at 891 cm^{-1} in the FTIR spectrum of the Tb-FAP/agar sample treated with UO_2^{2+} ions.[12,64] The –OH peak located at 3420 cm^{-1} in the FTIR spectrum shifted to 3395 cm^{-1} after the Tb-FAP/agar sample was treated with UO_2^{2+}. The C–H peak located at 1455 cm^{-1} almost disappeared. Moreover, the intensity of the PO_4^{3-} peaks located at 565, 604, 996, 1031 and 1093 cm^{-1} was sharply decreased. These changes could be attributed to the –OH, C–H, and PO_4^{3-} groups being chemically coordinated with UO_2^{2+}.[12] The –OH peak located at 3420 cm^{-1} in the FTIR spectrum shifted to 3392 cm^{-1} and 3394 cm^{-1} after the Tb-FAP/agar sample was treated with Cu^{2+} and Cr^{3+} ions, respectively. Moreover, the peaks related to the PO_4^{3-} group were shifted a little and the intensity decreased. These changes could be attributed to the –OH and PO_4^{3-} groups being chemically bound to Cu^{2+} and Cr^{3+}. The XPS spectra of the Tb-FAP/agar (Fig. 4a–c, respectively) showed the existence of U, Cu, and Cr on the Tb-FAP/agar sample after being treated with UO_2^{2+}, Cu^{2+}, and Cr^{3+} containing aqueous solutions, while no U, Cu, and Cr peaks were seen from the Tb-FAP/agar sample before being treated with UO_2^{2+}, Cu^{2+}, and Cr^{3+} containing solutions (Fig. 1b). The SEM images show the morphology of the Tb-FAP/agar sample being treated with UO_2^{2+}, Cu^{2+}, and Cr^{3+} ions (Fig. S12 a–c,† respectively). The surface morphology of the Tb-FAP/agar sample was more compact and rougher than before being treated with UO_2^{2+}, Cu^{2+}, and Cr^{3+} ions (Fig. S1†) with some fluffy substances attached to the surface of the Tb-FAP/agar. This finding indicated the formation of precipitates or complexes of uranium-, copper-, and chromium-based compounds on the surface of the Tb-FAP/agar. This result was supported by the XPS spectra of the Tb-FAP/agar (Fig. 4). The SEM images and FTIR and XPS spectral results confirmed the adsorption and coordination of UO_2^{2+}, Cu^{2+} and Cr^{3+} ions onto the Tb-FAP/agar sample. Thus, the observed luminescence quenching (Fig. 2b and 3) could be due to these adsorbed and coordinated ions.

The UV-vis absorption spectra of $(UO_2)(NO_3)_2$ and $Cr(NO_3)_3 \cdot 9H_2O$ aqueous solutions (Fig. S13†) indicated that they can absorb excitation light at 377 nm, which caused competition of UO_2^{2+} and Cr^{3+} with the Tb-FAP/agar sample for optical excitation. These results indicated that the competition for excitation light absorption could contribute to the luminescence quenching of the Tb-FAP/agar by UO_2^{2+} and Cr^{3+} ions. Meanwhile Cu^{2+} did not absorb light at 377 nm, which indicated that the competition for excitation light absorption by Cu^{2+} did not occur. In addition, no overlap was observed between the absorption spectrum of UO_2^{2+} and the emission spectrum of the Tb-FAP/agar, which revealed that the re-absorption of the emitted light by UO_2^{2+} did not happen. In contrast to UO_2^{2+}, the overlap existing between the absorption spectra of Cu^{2+} and Cr^{3+} ions and the emission spectrum of the Tb-FAP/agar sample demonstrated that the re-absorption of the emitted light may contribute to the luminescence quenching effect of the Tb-FAP/agar by Cu^{2+} and Cr^{3+} ions.

To further explore the luminescence quenching mechanism of the Tb-FAP/agar sample, its luminescence lifetime decay was recorded in the absence and presence of Cr^{3+}, Cu^{2+}, and UO_2^{2+} ions (Fig. 4d). The decay curves were fitted well by biexponential lifetime decay functions with the fitting parameters shown in Table S2.† The average

Table 1 Comparison of the LOD values of the Tb-FAP/agar nanocomposite with some reported sensors for UO_2^{2+}, Cu^{3+}, and Cr^{3+}

Metal ions	Sensors	LOD	Ref.
UO_2^{2+}	Co(II) metal–organic framework	700 nM	38
	ESF-1-Eu	292 μg L^{-1}	51
	Co–Zn isomorphous metal–organic frameworks	24 700 nM	25
	HNU-50	20 nM	52
	HOPO-CQD	6.53 μg L^{-1}	34
	CP1	5540 μg L^{-1}	53
	Zn(II) metal–organic framework	400 nM	54
	[EuL]	12 000 nM	55
	$[Eu_2(MTBC)(OH)_2(DMF)_3(H_2O)_4]\cdot 2DMF\cdot 7H_2O$	309.2 μg L^{-1}	49
	$[In_2(OH)_2(H_2TTHA)(H_2O)_2]_n$	420 μg L^{-1}	37
	Eu-MOF	900 nM	56
	Fluorescent polydopamine nanoparticles (FPD)	2100 μg L^{-1}	57
	$[Zn(HBTC)(BMIOPE)\cdot DMF\cdot H_2O]_n$	24 700 nM	25
	Tb-FHP/agar	7.95 nM (2.15 μg L^{-1})	This work
Cu^{2+}	YVO_4:Eu NPs	570 nM	58
	Ce^{3+}/Tb^{3+}-doped SrF_2 nanocrystals	2.2 nM	59
	Eu^{3+}-doped $KZnF_3$ nanoparticles	480 nM	60
	CDs/HAP-20	19 890 nM	61
	Probe CS	120.2 nM	62
	PVP@Gd_2O_3:Eu^{3+} NPs	3330 μg L^{-1}	27
	$[Eu_2(MTBC)(OH)_2(DMF)_3(H_2O)_4]\cdot 2DMF\cdot 7H_2O$	17.2 μg L^{-1}	49
	Tb-FHP/agar	3.94 nM (0.25 μg L^{-1})	This work
Cr^{3+}	PVP@Gd_2O_3:Eu^{3+} NPs	1660 μg L^{-1}	27
	Zn-MOF-1	2440 nM	26
	Zn3(bpdc)2(pdc)(DMF)·6DMF	25 100 nM	63
	$[Zn\ (HBTC)\ (BMIOPE)\cdot DMF\cdot H_2O]_n$	9700 nM	25
	Tb-FHP/agar	1.67 nM (0.087 μg L^{-1})	This work

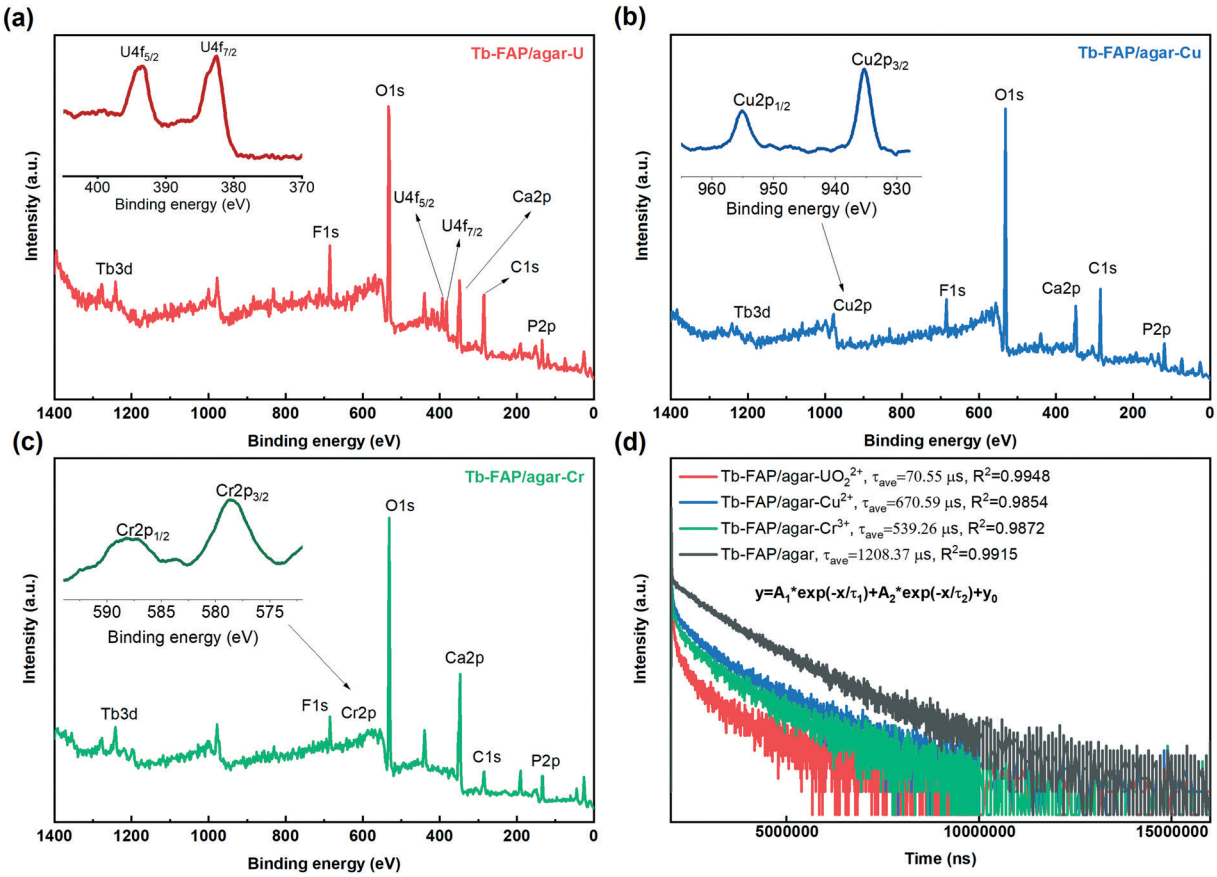

Fig. 4 XPS spectra of the Tb-FAP/agar after treatment with (a) UO_2^{2+}, (b) Cu^{2+}, and (c) Cr^{3+} accompanied with the insets showing the detailed XPS spectra of U 4f, Cu 2p, and Cr 2p, respectively. (d) The luminescence lifetime spectra of the Tb-FAP/agar sample recorded in the presence and absence of Cu^{2+}, Cr^{3+}, and UO_2^{2+} ions (λ_{ex} = 377 nm and λ_{em} = 543 nm).

luminescence lifetime of the Tb-FAP/agar sample was 1208.37 μs, while it dropped to 670.59 μs, 539.26 μs, and 70.55 μs in the presence of Cu^{2+}, Cr^{3+}, and UO_2^{2+}, respectively. The reduced luminescence lifetimes of the Tb-FAP/agar loaded with Cu^{2+}, Cr^{3+}, and UO_2^{2+} ions indicate that the electron transfer or energy transfer process from the Tb-FAP/agar to Cu^{2+}, Cr^{3+}, and UO_2^{2+}, causing faster exciton decays and shorter luminescence lifetimes, leads to the luminescence quenching. In the case of energy transfer, an overlap is needed between the emission spectra of donors and the absorption spectra of acceptors.[65] For UO_2^{2+} ions, no overlap was observed between the absorption spectrum of UO_2^{2+} and the emission spectrum of the Tb-FAP/agar (Fig. S13†), which shows that it is not energy transfer but rather the electron transfer process from Tb-FAP/agar to UO_2^{2+} that occurred. For Cu^{2+} and Cr^{3+}, an overlap was observed between the absorption spectra of Cu^{2+} and Cr^{3+} and the emission spectrum of the Tb-FAP/agar (Fig. S13†), which indicated that the energy transfer process occurred between the Tb-FAP/agar sample and Cu^{2+} and Cr^{3+} ions, leading to the luminescence quenching phenomenon.[66,67] Contrastingly, little change in the average luminescence lifetime of the Tb-FAP/agar sample was observed in the presence of the other tested metal ions (Table S3†). These results indicated that no electron transfer or energy transfer occurred between the Tb-FAP/agar sample and the other metal ions, and thus no luminescence quenching phenomenon occurred.

Based on the above results, the luminescence quenching mechanisms of the Tb-FAP/agar in the presence of Cu^{2+}, Cr^{3+}, and UO_2^{2+} ions were different from each other. The luminescence quenching mechanism of the Tb-FAP/agar with UO_2^{2+} involved the competition of excitation light absorption and the electron transfer between the Tb-FAP/agar sample and UO_2^{2+} ions. The luminescence quenching mechanism of the Tb-FAP/agar with Cu^{2+} involved the re-absorption of the emitted light from the Tb-FAP/agar sample and the energy transfer between the Tb-FAP/agar sample and Cu^{2+} ions. Meanwhile the luminescence quenching mechanism of the Tb-FAP/agar with Cr^{3+} ions included the competition of excitation light absorption, re-absorption of the emitted light from the Tb-FAP/agar sample, and energy transfer occurring between the Tb-FAP/agar sample and Cr^{3+} ions.

4. Conclusions

In summary, we developed a simple and green biomimetic route for the synthesis of a Tb-FAP/agar nanocomposite sample. The successful synthesis was confirmed by FT-IR,

XPS, TGA and XRD analysis. Both the F^- ion and agar can improve the luminescence intensity of the Tb-FAP/agar sample. The luminescence quenching constants K_{SV} of the Tb-FAP/agar sample were 2.47×10^5 M^{-1} for UO_2^{2+}, 6.77×10^5 M^{-1} for Cu^{2+}, and 1.37×10^6 M^{-1} for Cr^{3+}. The detection limits of the Tb-FAP/agar sample were 7.95 nM for UO_2^{2+}, 3.94 nM for Cu^{2+}, and 1.67 nM for Cr^{3+}. The large K_{SV} and low detection limit values of the Tb-FAP/agar sample indicated its excellent selectivity and sensitivity for detecting UO_2^{2+}, Cu^{2+}, and Cr^{3+} ions, which made it a promising luminescent sensor. The detection mechanism for UO_2^{2+} involved the competition of excitation light absorption and the electron transfer between the Tb-FAP/agar and UO_2^{2+} ions. For the Cu^{2+} detection, the quenching mechanism involved the re-absorption of emitted light and the energy transfer between the Tb-FAP/agar and Cu^{2+} ions. For the Cr^{3+} detection, the quenching mechanism included the competition of excitation light absorption, re-absorption of the emitted light from the Tb-FAP/agar, and energy transfer occurring between the Tb-FAP/agar and Cr^{3+} ions. Our findings indicated that luminescent RE-doped fluorapatites can be environmentally friendly designed and explored as potential luminescence sensors for environmental monitoring applications.

Conflicts of interest

The authors declared that they have no conflicts of interest to this work.

Acknowledgements

YM would like to acknowledge the support from the IIT startup funds. HL would like to acknowledge financial support from the China Scholarship Council (Grant No. CSC201908430311), the Natural Science Foundation of Hunan Province (Grant No. 2018JJ3420), the Research Foundation of Education Bureau of Hunan Province (Grant No. 18A233), and the Opening Project of Cooperative Innovation Center for Nuclear Fuel Cycle Technology and Equipment, University of South China.

References

1 X. Zhang, Q. Xing, L. Liao and Y. Han, Effect of the Fluorine Substitution for –OH Group on the Luminescence Property of Eu^{3+} Doped Hydroxyapatite, *Crystals*, 2020, **10**, 191.

2 Q.-Q. Zhang, Y.-J. Zhu, J. Wu, Y.-T. Shao, A.-Y. Cai and L.-Y. Dong, Ultralong Hydroxyapatite Nanowire-Based Filter Paper for High-Performance Water Purification, *ACS Appl. Mater. Interfaces*, 2019, **11**, 4288–4301.

3 I. Neacsu, E. Stoica, B. Vasile and E. Andronescu, Luminescent Hydroxyapatite Doped with Rare Earth Elements for Biomedical Applications, *Nanomaterials*, 2019, **9**, 239.

4 C. Wang, K.-J. Jeong, J. Kim, S. W. Kang, J. Kang, I. H. Han, I.-W. Lee, S.-J. Oh and J. Lee, Emission-tunable probes using terbium(III)-doped self-activated luminescent hydroxyapatite for in vitro bioimaging, *J. Colloid Interface Sci.*, 2021, **581**, 21–30.

5 A. Escudero, M. E. Calvo, S. Rivera-Fernández, J. M. de la Fuente and M. Ocaña, Microwave-Assisted Synthesis of Biocompatible Europium-Doped Calcium Hydroxyapatite and Fluoroapatite Luminescent Nanospindles Functionalized with Poly(acrylic acid), *Langmuir*, 2013, **29**, 1985–1994.

6 J. Stouwdam and F. Veggel, Near-infrared Emission of Redispersible Er^{3+}, Nd^{3+}, and Ho^{3+} Doped LaF_3 Nanoparticles, *Nano Lett.*, 2002, **2**, 733–737.

7 P. Sobierajska and R. J. Wiglusz, Influence of the grain sizes on Stokes and anti-Stokes fluorescence in the Yb^{3+} and Tb^{3+} ions co-doped nanocrystalline fluorapatite, *J. Alloys Compd.*, 2019, **785**, 808–818.

8 V.-H. Pham, H. N. Van, P. D. Tam and H. N. T. Ha, A novel 1540 nm light emission from erbium doped hydroxyapatite/β-tricalcium phosphate through co-precipitation method, *Mater. Lett.*, 2016, **167**, 145–147.

9 A. Yusoff, M. N. Salimi and M. Jamlos, Synthesis of Superparamagnetic Hydroxyapatite Core-Shell Nanostructure by a Rapid Sol-Gel Route, *e-J. Surf. Sci. Nanotechnol.*, 2017, **15**, 121–126.

10 M. Su, D. C. W. Tsang, X. Ren, Q. Shi, J. Tang, H. Zhang, L. Kong, L. A. Hou, G. Song and D. Chen, Removal of U(VI) from nuclear mining effluent by porous hydroxyapatite: Evaluation on characteristics, mechanisms and performance, *Environ. Pollut.*, 2019, **254**, 112891.

11 O. A. Graeve, R. Kanakala, A. Madadi, B. C. Williams and K. C. Glass, Luminescence variations in hydroxyapatites doped with Eu^{2+} and Eu^{3+} ions, *Biomaterials*, 2010, **31**, 4259–4267.

12 N. Zheng, L. Yin, M. Su, Z. Liu, D. C. W. Tsang and D. Chen, Synthesis of shape and structure-dependent hydroxyapatite nanostructures as a superior adsorbent for removal of U(VI), *Chem. Eng. J.*, 2020, **384**, 123262.

13 G. K. Lim, J. Wang, S. C. Ng, C. H. Chew and L. M. Gan, Processing of hydroxyapatite via microemulsion and emulsion routes, *Biomaterials*, 1997, **18**, 1433–1439.

14 Z. Chen, B. Wu, X. Huang, X. Li and Y. Lin, Biomimetic Synthesis of Hydroxyapatite in Presence of Imidazole-4,5-dicarboxylic Acid Grafted Chitosan for Removing Chromium(VI), *J. Nanotechnol.*, 2018, **2018**, 1–7.

15 C. H. Fang, Y. W. Lin, F. H. Lin, J. S. Sun, Y. H. Chao, H. Y. Lin and Z. C. Chang, Biomimetic Synthesis of Nanocrystalline Hydroxyapatite Composites: Therapeutic Potential and Effects on Bone Regeneration, *Int. J. Mol. Sci.*, 2019, **20**, 6002.

16 S. Cheng, Z. Wang, K. Sun, J. Dong and X. Li, Biomimetic fabrication of mulberry-like nano-hydroxyapatite with high specific surface area templated by dual-hydrophilic block copolymer, *Ceram. Int.*, 2017, **43**, 13430–13437.

17 Y. Ma, J. Zhang, S. Guo, J. Shi, W. Du, Z. Wang, L. Ye and W. Gu, Biomimetic mineralization of nano-sized, needle-like hydroxyapatite with ultrahigh capacity for lysozyme adsorption, *Mater. Sci. Eng., C*, 2016, **68**, 551–556.

18 Y. Chu, J. Hou, C. Boyer, J. J. Richardson, K. Liang and J. Xu, Biomimetic synthesis of coordination network materials: Recent advances in MOFs and MPNs, *Appl. Mater. Today*, 2018, **10**, 93–105.
19 M. A. Meyers, P.-Y. Chen, M. I. Lopez, Y. Seki and A. Y. M. Lin, Biological materials: A materials science approach, *J. Mech. Behav. Biomed. Mater.*, 2011, **4**, 626–657.
20 M. S. Hong, G.-M. Choi, J. Kim, J. Jang, B. Choi, J. K. Kim, S. Jeong, S. Leem, H. Y. Kwon, H. B. Hwang, H. G. Im, J. U. Park, B.-S. Bae and J. Jin, Biomimetic Chitin–Silk Hybrids: An Optically Transparent Structural Platform for Wearable Devices and Advanced Electronics, *Adv. Funct. Mater.*, 2017, **28**, 1705480.
21 R. Andre, M. N. Tahir, F. Natalio and W. Tremel, Bioinspired synthesis of multifunctional inorganic and bio-organic hybrid materials, *FEBS J.*, 2012, **279**, 1737–1749.
22 K. Liang, R. Wang, M. Boutter, C. M. Doherty, X. Mulet and J. J. Richardson, Biomimetic mineralization of metal-organic frameworks around polysaccharides, *Chem. Commun.*, 2017, **53**, 1249–1252.
23 N. Hammi, S. El Hankari, N. Katir, N. Marcotte, K. Draoui, S. Royer and A. El Kadib, Polysaccharide templated biomimetic growth of hierarchically porous metal-organic frameworks, *Microporous Mesoporous Mater.*, 2020, **306**, 110429.
24 J. Watanabe and M. Akashi, Novel Biomineralization for Hydrogels: Electrophoresis Approach Accelerates Hydroxyapatite Formation in Hydrogels, *Biomacromolecules*, 2006, **7**, 3008–3011.
25 N. N. Chen, A serial of 2D Co-Zn isomorphous metal–organic frameworks for photodegradation and luminescent detection properties, *Appl. Organomet. Chem.*, 2020, **34**, e5743.
26 X.-Y. Guo, F. Zhao, J. Liu, Z. Liu and Y.-Q. Wang, An ultrastable zinc(II)-organic framework as a recyclable multi-responsive luminescent sensor for Cr(III), Cr(VI) and 4-nitrophenol in the aqueous phase with high selectivity and sensitivity, *J. Mater. Chem. A*, 2017, **5**, 20035–20043.
27 M. Singh, N. Vashistha and A. Chandra, HSA functionalized Gd_2O_3:Eu^{3+} nanoparticles as MRI contrast agent and potential luminescent probe for Fe^{3+}, Cr^{3+}, Cu^{2+} detection in water, *New J. Chem.*, 2020, **44**, 14211–14227.
28 Y. Yue, J. Gu, J. Han, Q. Wu and J. Jiang, Effects of cellulose/salicylaldehyde thiosemicarbazone complexes on PVA based hydrogels: Portable, reusable, and high-precision luminescence sensing of Cu^{2+}, *J. Hazard. Mater.*, 2021, **401**, 123798.
29 D. Ghosh and M. N. Luwang, Selective detection of Fe^{3+}, Cr^{3+} and Cu^{2+} in water using highly luminescent Gd_2O_3:Eu^{3+} nanoparticles, *J. Lumin.*, 2016, **171**, 1–8.
30 L. Zhao, C. Ortiz Jr., Y. Huang, H. Zhou, A. Adeleye, S. Mazer and A. Keller, GC-TOF-MS based metabolomics and ICP-MS based metallomics of cucumber (Cucumis sativus) fruits reveal alteration of metabolites profile and biological pathway disruption induced by nano copper, *Environ. Sci.: Nano*, 2016, **3**, 1114–1123.
31 A. J. Stirling and W. D. Westwood, Detection of sputtered atoms by atomic absorption spectroscopy, *J. Phys. D: Appl. Phys.*, 1971, **4**, 246–252.
32 Y. Liang, B. Deng, C. Shen, X. Qin and S. Liang, Determination of the binding sites and binding constants between Pb(II) and DNA using capillary electrophoresis combined with electrothermal atomic absorption spectrometry, *J. Anal. At. Spectrom.*, 2014, **30**, 903–908.
33 J. Zhang, F. Cheng, J. Li, J.-J. Zhu and Y. Lu, Fluorescent nanoprobes for sensing and imaging of metal ions: Recent advances and future perspectives, *Nano Today*, 2016, **11**, 309–329.
34 Z. Zhang, D. Zhang, C. Shi, W. Liu, L. Chen, M. Yu, J. Diwu, J. Li and S. Wang, 3,4-Hydroxypyridinone-Modified Carbon Quantum Dot as a Highly Sensitive and Selective Fluorescent Probe for Rapid Detection of Uranyl Ions, *Environ. Sci.: Nano*, 2019, **6**, 1457–1465.
35 W. Liu, X. Dai, Z. Bai, Y. Wang, Z. Yang, L. Zhang, L. Xu, L. Chen, Y. Li, D. Gui, J. Diwu, J. Wang, R. Zhou, Z. Chai and S. Wang, Highly Sensitive and Selective Uranium Detection in Natural Water Systems Using a Luminescent Mesoporous Metal–Organic Framework Equipped with Abundant Lewis Basic Sites: A Combined Batch, X-ray Absorption Spectroscopy, and First Principles Simulation Investigation, *Environ. Sci. Technol.*, 2017, **51**, 3911–3921.
36 D. Xu, L. Chen, X. Dai, B. Li, Y. Wang, W. Liu, J. Li, Y. Tao, Y. Wang, Y. Liu, G. Peng, R. Zhou, Z. Chai and S. Wang, A Porous Aromatic Framework Functionalized with Luminescent Iridium(III) Organometallic Complexes for Turn-On Sensing of $^{99}TcO_4^-$, *ACS Appl. Mater. Interfaces*, 2020, **12**, 15288–15297.
37 N. Du, J. Song, S. Li, Y.-X. Chi, F.-Y. Bai and Y.-H. Xing, A Highly Stable 3D Luminescent Indium–Polycarboxylic Framework for the Turn-off Detection of UO_2^{2+}, Ru^{3+}, and Biomolecule Thiamines, *ACS Appl. Mater. Interfaces*, 2016, **8**, 28718–28726.
38 W. Chen, X.-L. Meng, G.-L. Zhuang, Z. Wang, M. Kurmoo, Q. Zhao, X.-P. Wang, S. Rong, C.-H. Tung and D. Sun, A superior fluorescent sensor for Al^{3+} and UO_2^{2+} based on Co(II) metal–organic framework with exposed Lewis basic pyrimidyl site, *J. Mater. Chem. A*, 2017, **5**, 13079–13085.
39 M. Bagheri and M. Masoomi, Sensitive Ratiometric Fluorescent Metal-Organic Framework Sensor for Calcium Signaling in Human Blood Ionic Concentration Media, *ACS Appl. Mater. Interfaces*, 2020, **12**, 4625–4631.
40 W. Liu, X. Dai, Y. Wang, L. Song, L. Zhang, D. Zhang, J. Xie, L. Chen, J. Diwu, J. Wang, Z. Chai and S. Wang, Ratiometric Monitoring of Thorium Contamination in Natural Water Using a Dual-Emission Luminescent Europium Organic Framework, *Environ. Sci. Technol.*, 2019, **53**, 332–341.
41 X. Guo, Q. Liu, J. Liu, H. Zhang, J. Yu, R. Chen, D. Song, R. Li and J. Wang, Magnetic metal-organic frameworks/carbon dots as a multifunctional platform for detection and removal of uranium, *Appl. Surf. Sci.*, 2019, **491**, 640–649.
42 L. Wang, Y. Wang, W. Li, W. Zhi, Y. Liu, L. Ni and Y. Wang, Recyclable DNA-Derived Polymeric Sensor: Ultrasensitive Detection of Hg(II) Ions Modulated by Morphological Changes, *ACS Appl. Mater. Interfaces*, 2019, **11**, 40575–40584.

43 M. Witzler, P. F. Ottensmeyer, M. Gericke, T. Heinze, E. Tobiasch and M. Schulze, Non-Cytotoxic Agarose/Hydroxyapatite Composite Scaffolds for Drug Release, *Int. J. Mol. Sci.*, 2019, **20**, 3565.

44 D. V. Milojkov, O. F. Silvestre, V. D. Stanić, G. V. Janjić, D. R. Mutavdžić, M. Milanović and J. B. Nieder, Fabrication and characterization of luminescent Pr^{3+} doped fluorapatite nanocrystals as bioimaging contrast agents, *J. Lumin.*, 2020, **217**, 116757.

45 J. Liu, C. Zhao, Z. Zhang, J. Liao, Y. Liu, X. Cao, J. Yang, Y. Yang and N. Liu, Fluorine effects on U(VI) sorption by hydroxyapatite, *Chem. Eng. J.*, 2016, **288**, 505–515.

46 X. Li, Z. Liu, K. Luo, X. Yin, X. Lin and C. Zhu, Biomimetic Synthesis of Ag_2Se Quantum Dots with Enhanced Photothermal Properties and as "Gatekeepers" to Cap Mesoporous Silica Nanoparticles for Chemo–Photothermal Therapy, *Chem. – Asian J.*, 2019, **14**, 155–161.

47 J. Lakowicz and B. Masters, Principles of Fluorescence Spectroscopy, Third Edition, *J. Biomed. Opt.*, 2008, **13**, 029901.

48 J. M. Han, M. Xu, B. Wang, N. Wu, X. Yang, H. Yang, B. J. Salter and L. Zang, Low Dose Detection of γ Radiation via Solvent Assisted Fluorescence Quenching, *J. Am. Chem. Soc.*, 2014, **136**, 5090–5096.

49 W. Liu, Y. Wang, L. Song, M. A. Silver, J. Xie, L. Zhang, L. Chen, J. Diwu, Z. Chai and S. Wang, Efficient and selective sensing of Cu^{2+} and UO_2^{2+} by a europium metal-organic framework, *Talanta*, 2019, **196**, 515–522.

50 T.-Y. Gu, M. Dai, D. J. Young, Z.-G. Ren and J.-P. Lang, Luminescent Zn(II) Coordination Polymers for Highly Selective Sensing of Cr(III) and Cr(VI) in Water, *Inorg. Chem.*, 2017, **56**, 4668–4678.

51 S. Lee, K. Y. Kim, N. Y. Lim, J. H. Jung, J. H. Lee, M. Y. Choi and J. H. Jung, Terpyridine-based complex nanofibers with Eu^{3+} as a highly selective chemical probes for UO_2^{2+}, *J. Hazard. Mater.*, 2019, **378**, 120713.

52 X. Qin, W. Yang, Y. Yang, D. Gu, D. Guo and Q. Pan, A Zinc Metal–Organic Framework for Concurrent Adsorption and Detection of Uranium, *Inorg. Chem.*, 2020, **59**, 9857–9865.

53 Y. Wang, S. H. Xing, X. Zhang, C. H. Liu, B. Li, F. Y. Bai, Y. H. Xing and L. X. Sun, A family of functional Ln-organic framework constructed by iodine-substituted aromatic polycarboxylic acid for turn-off sensing of UO_2^{2+}, *Appl. Organomet. Chem.*, 2019, **33**, e4898.

54 J.-X. Hou, J.-P. Gao, J. Liu, X. Jing, L.-J. Li and J.-L. Du, Highly selective and sensitive detection of Pb^{2+} and UO_2^{2+} ions based on a carboxyl-functionalized Zn(II)-MOF platform, *Dyes Pigm.*, 2018, **160**, 159–164.

55 P. Harvey, A. Nonat, C. Platas-Iglesias, L. S. Natrajan and L. Charbonnière, Sensing Uranyl(VI) Ions by Coordination and Energy Transfer to a Luminescent Europium(III) Complex, *Angew. Chem.*, 2018, **57**, 9921–9924.

56 L. Li, S. Shen, J. Su, W. Ai, Y. Bai and H. Liu, Facile one-step solvothermal synthesis of a luminescent europium metal-organic framework for rapid and selective sensing of uranyl ions, *Anal. Bioanal. Chem.*, 2019, **411**, 4213–4220.

57 Z. Wang, C. Xu, Y. Lu, G. Wei, G. Ye, T. Sun and J. Chen, Microplasma electrochemistry controlled rapid preparation of fluorescent polydopamine nanoparticles and their application in uranium detection, *Chem. Eng. J.*, 2018, **344**, 480–486.

58 C. Chen, J. Li, C. Li, H. Huang, C. Liang, Y. Lou, D. Liu, Z. Wang, Z. Shi and S. Feng, Facile Synthesis of Water-Soluble YVO_4:Eu Nanoparticles for Cu^{2+} Detection in Aqueous Solution, *ChemistrySelect*, 2016, **1**, 1417–1420.

59 S. Sarkar, M. Chatti, V. Adusumalli and V. Mahalingam, Highly Selective and Sensitive Detection of Cu^{2+} Ions Using Ce(III)/Tb(III)-Doped SrF_2 Nanocrystals as Fluorescent Probe, *ACS Appl. Mater. Interfaces*, 2015, **7**, 25702–25708.

60 S. Sarkar, M. Chatti and V. Mahalingam, Highly luminescent colloidal Eu^{3+}–doped $KZnF_3$ nanoparticles for the selective and sensitive detection of Cu(II) ions, *Chem. – Eur. J.*, 2014, **20**, 3311–3316.

61 R.-Z. Jing, J.-M. Yin, X.-R. Zeng, S.-R. Zhao, Y.-N. Xue, J.-K. Liu, X.-M. Zhang and X.-H. Yang, Assembly and copper ions detection of highly sensible and stable carbon dots/hydroxyapatite fluorescence probe, *Mater. Technol.*, 2019, **34**, 674–682.

62 Y. Gao, C. Zhang, S. Peng and H. Chen, A fluorescent and colorimetric probe enables simultaneous differential detection of Hg^{2+} and Cu^{2+} by two different mechanisms, *Sens. Actuators, B*, 2017, **238**, 455–461.

63 X. Meng, M. Wei, H. Wang, H. Zang and Z. Zhou, Multifunctional luminescent Zn(II)-based metal–organic framework for high proton-conductivity and detection of Cr^{3+} ions in the presence of mixed metal ions, *Dalton Trans.*, 2018, **47**, 1383–1387.

64 J. Huynh, R. Palacio, F. Safizadeh, G. Lefèvre, M. Descostes, E. Lilian, N. Guignard, J. Rousseau, S. Royer, E. Tertre and I. Batonneau-Gener, Adsorption of Uranium over NH_2-Functionalized Ordered Silica in Aqueous Solutions, *ACS Appl. Mater. Interfaces*, 2017, **9**, 15672–15682.

65 Y. Liu, X. Tang, T. Zhu, M. Deng and F. Qiu, All–inorganic $CsPbBr_3$ perovskite quantum dots as photoluminescent probe for ultrasensitive Cu^{2+} detection, *J. Mater. Chem. C*, 2018, **6**, 4793–4799.

66 T.-Y. Gu, M. Dai, D. J. Young, Z.-G. Ren and J.-P. Lang, Luminescent Zn(II) Coordination Polymers for Highly Selective Sensing of Cr(III) and Cr(VI) in Water, *Inorg. Chem.*, 2017, **56**, 4668–4678.

67 S. Sarkar, M. Chatti, V. N. Adusumalli and V. Mahalingam, Highly Selective and Sensitive Detection of Cu^{2+} Ions Using Ce(III)/Tb(III)-Doped SrF_2 Nanocrystals as Fluorescent Probe, *ACS Appl. Mater. Interfaces*, 2015, **7**, 25702–25708.